Designed Synthesis of STA-30: A Small Pore Zeolite Catalyst with Topology Type SWY

Ruxandra G. Chitac,[1] Jonathan Bradley,[2] Nicholas McNamara,[3] Alvaro Mayoral,[4,5,6]

Alessandro Turrina[7,*] and Paul A. Wright[1,*]

[1] EaStCHEM School of Chemistry, University of St Andrews, St Andrews, KY16 9ST, United Kingdom.

[2] Johnson Matthey Technology Centre, Reading, RG4 9NH, United Kingdom.

[3] Johnson Matthey, Wayne, Pennsylvania 19087, United States.

[4] Instituto de Nanociencia y Materiales de Aragon (INMA), Spanish National Research Council (CSIC)-University of Zaragoza, Zaragoza, 50009, Spain.

[5] Laboratorio de Microscopias Avanzadas (LMA), University of Zaragoza, Zaragoza, 50018, Spain.

[6] Center for High-Resolution Electron Microscopy (CħEM), School of Physical Science and Technology, ShanghaiTech University, Pudong, 201210, Shanghai.

[7] Johnson Matthey Technology Centre, Billingham, TS23 1LB, United Kingdom.

Corresponding author emails: paw2@st-andrews.ac.uk, alessandro.turrina@matthey.com

ABSTRACT

Small pore aluminosilicate zeolites are attractive targets for synthesis because of their activity as catalysts in important reactions, including ammonia-mediated selective catalytic reduction (SCR) of NO_x in auto-exhaust emissions. Such a zeolite with SWY framework type, previously observed as a silicoaluminophosphate, has been prepared highly crystalline via designed syntheses employing organic 1,8-(1,4-diazabicyclo[2.2.2]octane)octyl (diDABCO-C8) and K^+ cations as templates. STA-30 (St Andrews microporous material 30) is an ABC-6 structure in the erionite-offretite family of zeolites that exhibits the 12-layer stacking sequence AABAABAACAAC. The framework, which can be prepared with controllable Si/Al ratio, possesses columns of alternating *d6r* units and *can* cages, the latter oriented to give an inter-column pore space comprising *gme* cages and *swy* cages connected via 8Rs. DiDABCO-C8 cations fill the *swy* cages of as-prepared STA-30 while K^+ cations display high occupancy in the *can* cages. Removal of template by calcination, followed by ammonium ion exchange

of K^+ cations residing outside the *can* cages and subsequent deammoniation, gives a highly crystalline zeolite ($K_3H_6Al_9Si_{72}O_{144}$, $P6_3/mmc$, a = 12.9922(9) Å, c = 29.9624(12) Å) with solid acidity shown by solid state ^{1}H MAS NMR. Upon hydration, a portion of the Al adopts octahedral geometry, as demonstrated by two sharp resonances at −2.0 ppm and −3.1 ppm in the ^{27}Al MAS NMR. These octahedral species can be converted back to tetrahedral Al by ammonium exchange and are interpreted as distinct hydrated framework Al sites. The activated K,H-STA-30 is a small pore solid acid with a three-dimensionally connected micropore volume of 0.31 $cm^3\ g^{-1}$. In the copper-loaded form it is an active catalyst for the SCR of NO by ammonia.

INTRODUCTION

The discovery and development of new zeolitic aluminosilicates continues to add to the pool of potential adsorbents and catalysts for industrial processes. Among these, small pore materials (with pores of free diameters from 3 – 4 Å) have found widespread use and potential applications in air separation and carbon capture, and in the important catalytic processes of the conversion of methanol to light olefins (the MTO reaction) and the selective catalytic reduction (SCR) of NO emissions from diesel engines.[1,2]

For the lattermost reaction, Cu-exchanged chabazite zeolite SSZ-13 (which has the topology type CHA) is the industry standard,[3,4] giving good conversion, selectivity and hydrothermal stability over a range of conditions. Nevertheless, other small pore zeolites also show commercial applicability (such as SSZ-39(AEI))[5,6] and, in general, zeolites with smaller pore sizes perform better than those with medium or large pores in this reaction.[4,7] For example, SSZ-13 is a member of the ABC-6 family of zeolite structures. In this family, the frameworks are built from the stacking of layers of 6-membered rings (6Rs) parallel to the *ab*-plane, connected by 4Rs along the *c*-direction. There are three different positions for these 6Rs, related through translation in the hexagonal *ab*-plane, centred at *x*, *y* coordinates of (0,0), (⅔,⅓) and (⅓,⅔) and denoted A, B and C. Each stacking sequence within this family can then be described using these letters. The CHA topology type, for example, has the AABBCC stacking sequence, giving rise to a single type of cage, the *cha* cage, connected to six others via 8-membered ring openings. The ABC-6 family exhibits many different materials: the 'Zeolite Atlas'[8] reports 25 materials discovered to date, either natural or synthetic, and new structures continue to be reported.[9] Recently, Li *et al.* analysed this structural family via a high-throughput computational study and concluded that there are at least 1150 energetically viable ABC-6 topologies that could be feasible targets for synthesis.[10]

The ABC-6 structure types can be prepared with different framework compositions, so that as well as aluminosilicate zeolites, many aluminophosphate (AlPO) zeotypes have been observed. For example, the silicoaluminophosphate (SAPO) analogue of chabazite, SAPO-34,[11] is widely used in the MTO reaction,[12] and has good activity as Cu-SAPO-34 in ammonia SCR of NO.[13] However, the (hydro)thermal stability at low temperatures of the Cu-SAPOs is lower than that of high silica Cu-zeolites under the conditions of SCR, where the required lifetimes are very long, and therefore aluminosilicates are the preferred catalysts for this reaction.[14] Nevertheless, structures observed as AlPOs (and SAPOs), if prepared as zeolites, can be of considerable catalytic interest.

Of the 25 reported zeotypes of the ABC-6 family, 11 have been prepared as both aluminosilicates and AlPOs (SAPOs),[8] which indicates the feasibility of compositional 'crossover' and demonstrates that ABC-6 structures known to occur as AlPOs can be candidates for synthesis as zeolites. Further, seven ABC-6 topology types were prepared for the first time as AlPOs or SAPOs, and while two of these have subsequently been synthesised as aluminosilicates, AFX – SAPO-56 and later SSZ-16,[15,16] and recently AFT – AlPO-52 and then SSZ-112 (highly faulted),[17,18] the remainder are attractive targets. The topology type SWY, recently prepared as SAPO STA-20,[19] is one of these. The SWY structure has the 12-layer stacking sequence AABAABAACAAC and contains parallel columns of *can* cages and *d6rs* and of *gme* and larger *swy* cages, with the latter two types of cages connected via 8R windows. It is therefore closely related to the ERI and OFF structures (also ABC-6 structures, with stacking sequences AABAAC and AAB) and all are based on structural units of columns of alternating *d6r*s and *can* cages (Figure 1). The difference lies in the orientation of the *can* cages and as a result the types of larger cages (ERI – *eri*; OFF - *gme*) or channels (OFF) that are present. Hence, we thought that a zeolite with this structure would be a good candidate for catalytic testing in the SCR reaction and so it offered an excellent target for designed synthesis.

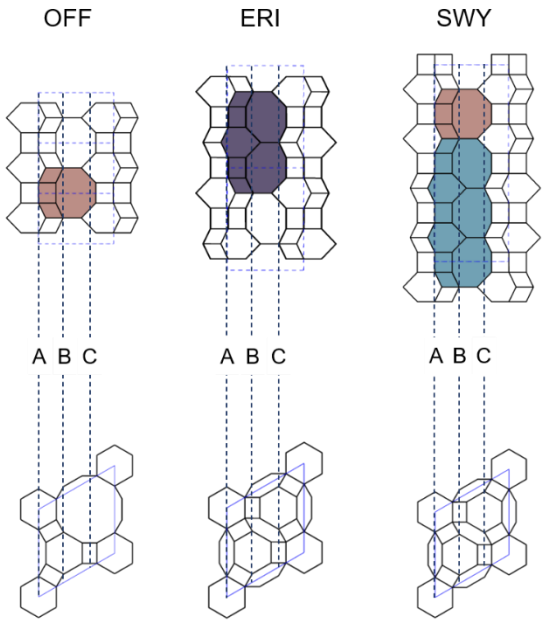

Figure 1. The layer stacking sequence and specific cages in the OFF, ERI and SWY frameworks (*gme* cage – light brown, *eri* cage – purple, *swy* cage – blue)

The designed synthesis of zeolites and zeotypes has achieved some notable successes in recent years, usually through the design of organic structure directing agents (OSDAs) that are a close fit to cages within the framework. It has been established that alkylammonium and other organic cations can be highly selective templates for zeolites during their hydrothermal crystallisation, and that it is possible to analyse and model potential new frameworks and assess their synthetic viability.[20–23] Therefore, a number of groups have adopted computational methodology to design a template for a framework of given structure and composition and then to prepare it. Examples include the synthesis of STA-18, topology type SFW, previously prepared highly faulted as the aluminosilicate SSZ-52 but realised as a SAPO by a retrosynthetic approach using modelling,[24] and the aluminosilicate ITQ-47, isostructural with the mineral *boggsite* and prepared via a phosphazene template.[25] Schmidt *et al.* were able to prepare a pure silica STW for the first time by template design[26] and Shi *et al.* reported modelling studies to develop new templates for the same structure.[27] Furthermore, X. Hong et al.[28] were able to prepare an aluminosilicate with the IFW topology, which had previously been directly prepared only as the germanosilicate ITQ-24 or borosilicate or pure silica versions,[29,30] via computational assessment of candidate pyrrolidine-based OSDAs. Recently, Jo and S. B. Hong have reported a designed template synthesis of a zeolite with a previously unrealised topology type that had been predicted by consideration of hypothetical variants of the brewsterite zeolite structure.[31]

Whereas in SAPOs the use of organic templates is sufficient to guide the synthesis, in aluminosilicate syntheses there is a greater variability in gel compositions and inorganic cations (and anions, in fluoride syntheses). Therefore, the effect of these inorganic parameters is also important and the metal cations contribute to determining which structure crystallises.[32] For example, Hong *et al.* made use of the effects of Sr^{2+} and Ba^{2+} cations in addition to those of Na^{+} and tetraethylammonium ions to guide syntheses within the extended RHO series of zeolites.[33,34]

Here we report the designed synthesis of the aluminosilicate form of SWY using a combination of computational analysis of template-framework interactions and careful control of the parameters of the gel composition and the hydrothermal synthesis. The successful synthesis has been confirmed by advanced characterisation techniques and the catalytic performance of the stable calcined form, once Cu-exchanged, has been investigated in the ammonia SCR of NO.

EXPERIMENTAL

Synthesis

STA-30 type materials were prepared in stainless steel autoclaves with Teflon liners. First of all, the Al source – aluminium isopropoxide (98%, Acros Organics) or aluminium hydroxide (>76.5%, Alfa Aesar) was dissolved in a solution of tetrapropylammonium hydroxide (40%, SACHEM). Ludox HS-40 (Sigma Aldrich) was added and the mixture allowed to homogenise for at least 1.5 h. If the synthesis was carried out in large liners (>50 mL), then the isopropyl alcohol formed was allowed to evaporate by heating the gel (confirmed by monitoring weight loss and the water content was adjusted to maintain the desired H_2O/SiO_2 ratio in the gel). The gel was aged for 20 h at 368 K. Aqueous solutions of 1,*n*-(diazabicyclo[2.2.2]octane)alkyl bromide (diDABCO-C*n*)Br_2 (for n = 7, 9, 10, synthesis provided in the Supporting Information (SI), Section 1, and for n = 8, provided by Alfa Aesar) and potassium hydroxide were prepared and added to the aged gel dropwise. The resulting mixture was stirred at RT for a further 2 h, after which the autoclaves were rotated at 60 rpm and heated at 393 – 413 K for 5 days. At the 1.5 L scale, the rotation of the autoclave was replaced by mechanical stirring at 300 rpm using a pitched blade type of impeller. The product was recovered by centrifugation and washed with deionised water. A typical gel composition was: 1.0 SiO_2: 0.05 Al_2O_3: 0.10 KOH: 0.12 (diDABCO-C8)Br_2: 0.4 TPAOH: 20 H_2O. The amount of Al source, KOH, H_2O and (diDABCO-C8)Br_2 could be varied to some extent without affecting the purity of the product.

Ion exchange and activation procedure

As-prepared materials were calcined in flowing air by heating the sample at 823 K for a minimum of 12 h. The calcined materials were then ion exchanged with a solution of 1M ammonium chloride at RT. Ion exchange reached equilibrium after 1 h of stirring solution and zeolite in the ratio of 100 mL g^{-1}. After one hour of ion exchange, the sample was filtered and a fresh batch of 1M NH_4Cl solution added in the same ratio. The mixture was stirred for a further hour. It was found that performing the ion exchange at elevated temperatures (up to 363 K) did not affect the maximum amount of K^+ that could be removed from STA-30. The H-form of the zeolite ('activated' material) was obtained by removing NH_3 by heating at up to 723 K for at least 12 h under a continuous flow of air.

For crystallographic purposes, the samples were dehydrated by packing them into 0.7 mm silica glass capillaries that were then attached to a glass vacuum line. The capillaries were heated up to 553 K for 10 h and kept under vacuum at about 5×10^{-5} mbar. They were then flame sealed to achieve an isolated environment.

Analytical methods

The phase purity, crystallinity and structure of as-prepared, calcined, and activated and dehydrated STA-30 were analysed by powder X-Ray diffraction (PXRD). For phase analysis, the data was collected in Bragg-Brentano geometry in the 2θ range 5−50°, via a primary monochromator, at 30 kV and 10 mA on a Bruker D2 diffractometer equipped with a LynxEye detector (using Cu $K_{\alpha 1}$ X-radiation, λ = 1.54059 Å, via a primary monochromator, step size 0.02°, time per step of 33 s). The sample was rotated at 15 rpm during the data collection to minimise preferred orientation. For structural analysis, patterns of the dehydrated materials were collected from sealed capillaries using a STOE STADI P diffractometer, also with Cu $K_{\alpha 1}$ radiation, in the 2θ range 5−70°. The capillaries were rotated rapidly during the collection.

Morphology and crystallite size were determined using images acquired with a field emission high resolution scanning electron microscope Jeol JSM-6700F or Jeol JSM-601LA after coating the samples with carbon.

Spherical aberration-corrected (C_s-corrected) annular dark-field scanning transmission electron microscopy (ADF-STEM) measurements were made on a FEI Titan 60−300 transmission electron microscope equipped with a high brightness Schottky X-FEG emitter and operated at 300 kV. The column was fitted with a CEOS spherical aberration corrector for the electron probe, which was aligned using a gold standard sample prior to every experiment. The microscope also incorporates a Gatan Tridiem energy filter and a Fischione HAADF detector. The half angle of illumination employed was

17.5 mrad. The values extracted for the different aberrations were A1 < 2 nm; A2 and B2 < 20 nm, C3 500 nm; S3 and A3 < 600 nm, allowing a measured probe size of 0.78 Å. The total time for each of the images presented here did not exceed 10 s with 1024 × 1024 pixels per micrograph. The electron current was kept below 10 pA, and the collection angle was set to 30 mrad (inner) and 200 mrad (outer). The images were collected using Gatan's DigitalMicrograph™ software. The samples were prepared for the microscope by grinding in presence of few drops of ethanol and deposition on to lacy carbon films supported on Cu grids. Image viewing and processing was performed using the public domain version of Gatan's DigitalMicrograph™ program with the addition of an Average Background Subtraction Filter (ABSF) filter written by Mitchell.[35]

Elemental compositions of materials discussed in this paper were determined using energy dispersive X-Ray spectroscopy (EDS) or X-ray fluorescence spectroscopy (XRF). EDS spectra were collected on a Jeol JSM-5600 instrument equipped with an Oxford Inca EDS system for compositional analysis. XRF spectra were collected on Bruker S8 WDXRF (wavelength-dispersive X-ray fluorescence) spectrometer. Thermogravimetric analysis (TGA) was carried out on a NETZSCH TG1000 M. Samples were heated up to 1073 K at a rate of 5 K min^{-1} in a dry air flow.

Solid state NMR spectra were acquired at a static magnetic field strength of either 9.4 T ($\nu_0(^1H)$ = 400 MHz) or 14.1 T ($\nu_0(^1H)$ = 600 MHz) on either a Bruker Avance III console using TopSpin 3.1 software or a Bruker Avance Neo console using TopSpin 4.0 software. Samples used for ^1H and ^1H-^{29}Si HETCOR were dried overnight at 623 K under vacuum and packed in a dry atmosphere. For ^{27}Al, the activated and NH_4-exchanged samples were stored overnight in a humid environment. Powdered samples were packed into zirconia MAS rotors with Kel-F caps. The rotors were spun using room-temperature purified compressed air. The spinning frequency was either 4 kHz (^{29}Si, activated sample), 8 kHz (^{29}Si, as-prepared sample), 10 kHz (^{13}C) or 14 kHz (^{27}Al, ^1H). Recycle delays were 0.1 s (^{27}Al, NH_4^+-exchanged sample), 0.4 s (^{27}Al, as-prepared and activated samples), 1.5 s (^{13}C), 5.5 s (^1H, NH_4^+-exchanged sample), 6.5 s (^1H, activated sample), 35.2 s (^{29}Si, activated sample) and 240 s (^{29}Si, as-prepared sample). The HETeronuclear chemical shift CORrelation (HETCOR) spectrum was recorded using cross polarisation (CP) with a contact time of 5 ms. For ^{13}C, the probe was tuned to 150.94 MHz and referenced to alanine CH_3 at 20.5 ppm. For ^{27}Al, the probe was tuned to 156.40 MHz and referenced to YAG at 0.0 ppm. For ^{29}Si, the probe was tuned to 119.23 MHz and referenced to kaolinite at −91.2 ppm. For ^1H, the probe was tuned to 600.22 MHz and referenced to d_{16}-adamantane at 1.73 ppm.

Solution NMR spectra were collected on either a Bruker AVIII 500 or Bruker AVII 400 spectrometer.

N_2 adsorption isotherms were measured at 77 K using a Micromeritics 3-Flex apparatus. Prior to measurement the samples were heated under vacuum at 623 K for 16 h to remove physisorbed water.

To prepare the material as a Cu catalyst for SCR, activated forms of STA-30 with two different Si/Al ratios were slurried with copper (II) acetate monohydrate (Shepherd) dissolved in de-mineralised water at 313 K for 4 h, to give a Cu loading of 3.33 wt%. The slurried samples were then dried in a static oven at 353 K for at least 16 h. The Cu-containing STA-30 samples were then calcined in air at 823 K for 4 h. The samples were then pelletized and loaded into an SCR test rig. A gas mixture consisting of 500 ppm NO, 14% O_2, 4.6% H_2O, 5% CO_2 and a balance of N_2 was passed over the catalyst at a space velocity of 90 h^{-1}. The samples were heated to 423 K in this gas mixture and when 423 K was reached, NH_3 was added into the gas mixture at 500 ppm and the samples were held for 30 minutes isothermally to equilibrate. The temperature was then increased from 423 to 773 K at 5 K min^{-1} while the outlet gas composition was monitored by FTIR.

Crystallography

Structure refinement was performed using the GSAS program suite through the EXPGUI user interface.[36] A starting model for the framework was taken from the International Zeolite Association database. The framework atomic positions were refined with geometric restraints for the T-O (T=Si or Al, bond length = 1.61 ± 0.02 Å) and O-O distances (bond length 2.63 ± 0.02 Å) to maintain the tetrahedral geometry around every T site.[37] The weight of the restraints was reduced during the refinement. The positions of K^+ cations within the framework were estimated based on published work on other related frameworks or through Fourier mapping. The background and thermal factors were refined separately due to their strong correlation. Structures in *.cif* files were simulated, visualised, and manipulated using CrystalMaker®.[38] Additional image editing was performed using the GIMP software.

Computational methodology

All calculations for modelling the OSDA inside the *swy* cages were performed using the Forcite module, available in BIOVIA Materials Studio 2020.[39] The COMPASS II forcefield was used with charges assigned separately to the template, cations and framework to achieve a neutral system.[40,41] As part of this study, geometry optimisation and molecular dynamics calculations were used to determine the suitability of different DABCO based molecules for templating the *swy*-cages of an

idealised silicate SWY framework converted to *P*1 symmetry. The fractional coordinates and unit cell were allowed to optimise during the geometry optimisation calculations. These calculations were performed using the 'Smart' algorithm with the following convergence thresholds: 10^{-4} kcal mol^{-1} for energy, 5×10^{-3} kcal mol^{-1} Å^{-1} for force, 5×10^{-3} GPa for stress and 5×10^{-5} for displacement. The molecular dynamics calculations were run using the NVE thermodynamic ensemble, with random initial velocities and a target temperature of 650 K. The time step of the simulation was 1 fs and the total time was 50 ps. Snapshots of the results were taken every 500 steps, obtaining in total 101 frames that were then geometry optimised to find the most stable structure generated by the molecular dynamics calculation. Finally, the lowest energy OSDA loaded structure was subjected to a 'Forcite Anneal' calculation in the temperature range 300 – 700 K, set up to perform 1000 dynamics steps per ramp, 5 ramps per cycle and 10 cycles in total. Each annealed structure was geometry optimised. The structure with the lowest energy resulting from this calculation was studied in detail. The binding energy was determined by calculating the difference between the total energy of the optimised templated structure and the total energy of the empty framework and the energy of the OSDA molecules in the conformation inside the cages.

Another value considered in determining the most favourable host-guest interaction was the torsion energy, which was determined as the difference in torsion energy between that of the OSDA molecule in ground state and in the conformation inside the *swy* cages.

First-principles calculations were performed using CASTEP version 8.0.[42] Calculations employed the Perdew-Burke-Ernzehorf (PBE) functional,[43] the Tkatchenko-Scheffler (TS) dispersion correction,[44] and on-the-fly generated ultrasoft pseudopotentials. For all geometry-optimisation calculations, a plane wave basis cut-off energy of 600 eV was used with a Monkhorst-Pack grid with a minimum k-point spacing of 0.05 Å^{-1}.[45] All atoms within the unit cell were allowed to relax during geometry optimisation, and the unit cell parameters were fixed. NMR shielding values were calculated using the GIPAW method[46] for the optimised structures, with a plane-wave cut-off energy of 700 eV, and a Monkhorst-Pack grid with a minimum k-point spacing of 0.05 Å^{-1}. The calculated shieldings, σ_{GIPAW}, were shifted by a reference value σ_{ref} of 328, such that the mean experimental and calculated chemical shifts coincided.

RESULTS AND DISCUSSION

The SWY topology type described in the Introduction was prepared for the first time as the silicoaluminophosphate, SAPO STA-20, using diDABCO-C6^{2+} and trimethylamine (TrMA) as organic structure directing agents. In that case, diDABCO-C6^{2+} was found to occupy the *swy* cages, along with TrMA, while additional TrMA acted as a template for the *gme* cages.[19] DiDABCO-type dicationic molecules therefore provided a promising starting point in the design of potential templates for the *swy* cage in an aluminosilicate SWY, although the amine is not expected to be a good co-template in zeolite synthesis because it is likely to be neutral at the high pH used.

The potential suitability of a series of diDABCO-Cn^{2+} molecules of different lengths (n = 6 –10) as templates for the *swy* cage in a SWY framework with composition SiO_2 was assessed through molecular dynamics calculations. The minimum energy location of the molecules of the different diDABCO-Cn^{2+} templates is shown in Figure 2 and the calculated energies of overall stabilisation are listed in Table 1. Even though the unit cell parameters were allowed to vary during the energy minimisations, they did not deviate significantly for structures with different OSDAs included (SI, Section 2, Figure S1). The diDABCO-C8^{2+} molecule was observed to be a better fit than diDABCO-C6^{2+} inside the *swy* cage, which is considerably shorter (at ~14.1 Å) than the length of the *swy* cage (~22.7 Å) - for the STA-20 SAPO this also occludes a TrMA molecule. Even though the length of diDABCO-C7^{2+} seemed more appropriate, it was diDABCO-C8^{2+} that conferred the strongest binding energy to the optimised structure (Table 1). Longer molecules in this family incurred energy costs from higher torsion energies (OSDA molecules in their ground state conformation are shown in the SI, Section 2, Figure S2). The binding energies derived from these calculations also show that OSDAs with an odd number of C atoms in the alkyl chains perform less well than those with an even number of C atoms. This appears to be due to the relative orientation of the DABCO end groups and the ends of the *swy* cage, and the resulting interactions between the end groups and the framework. Therefore, this modelling led to the choice of diDABCO-C8^{2+} as the best candidate template.

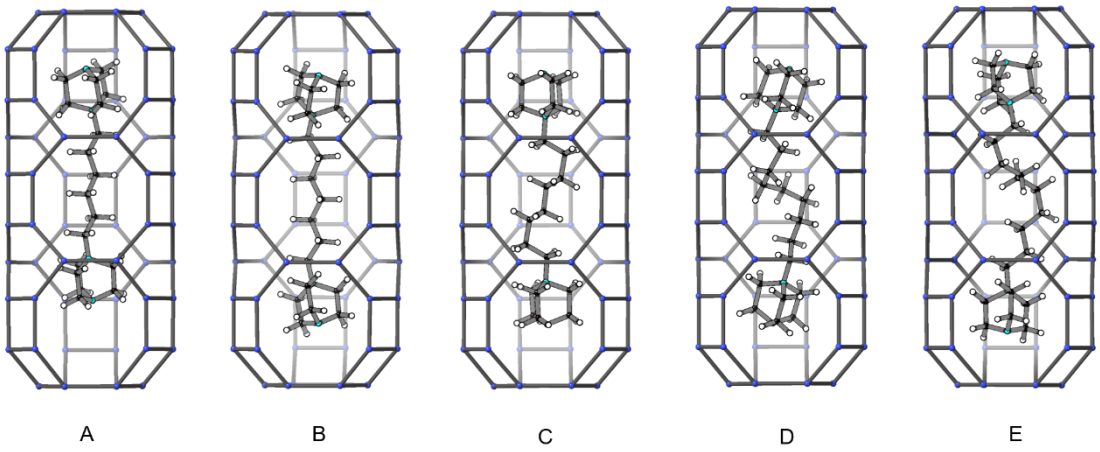

Figure 2. The fit of diDABCO-Cn^{2+} (n = 6 – 10, shown in order A-E) templates in the silicate SWY framework, modelled using molecular dynamic calculations.

Table 1. Results of molecular dynamics calculations on an ideal SWY silica framework, with molecules of diDABCO-Cn^{2+} fitted inside both *swy* cages of a unit cell.

n	**Binding energy** (kcal mol^{-1})	**ΔTorsion energy OSDA** (kcal mol^{-1})
6	–392.7	0.1
7	–386.3	0.1
8	–399.1	0.9
9	–392.3	1.1
10	–392.5	2.3

Beyond the choice of the OSDA, the synthetic conditions for targeting SWY were inspired by the gel composition (1.0 SiO_2: 0.05 Al_2O_3: 0.09 KOH: 0.10 RBr_2: 0.4 TPAOH: 16 H_2O) and conditions presented by Zhu *et al.* for the crystallisation of UZM-12, an aluminosilicate with the related ERI framework.[47] Both SWY and ERI frameworks belong to the ABC-6 family and have many building units in common, including the *can* cages, which are templated by K^+ cations. While in the work previously mentioned on UZM-12, the largest cage – *eri*, is templated by hexamethonium (HM^{2+}) molecules, this was replaced in our preparation by the diDABCO-C8^{2+} molecule designed as a template for the *swy* cage, as described above.

Syntheses were performed between 393 K and 423 K, using the 50 mL autoclaves, with tumbling. The gel composition was close to that of Sample 1 in Table 2. Notably, crystallisation at the higher temperature of 423 K resulted in ZSM-5 impurity, which can be attributed to the presence of TPA^+ cations added here as mineralising agents in the first step of gel formation.[48] Otherwise, the same material appeared to have been formed between 393 – 413 K (SEM images and PXRD patterns of these samples in the SI, Section 3, Figures S3 and S4). The PXRD pattern of the product crystallised at 413 K was compared with the patterns simulated for the SWY framework (using the structure of as-prepared STA-20), as well as for zeolites erionite, offretite and their intergrowth, zeolite T (Figure 3). The preparation of these materials is detailed in the SI – Section 4. The patterns of these related materials are very similar, with many peaks in common, but there are peaks characteristic of the SWY structure because of the extended *c*-axis, including the (101) reflection at 8.3° 2θ. It immediately appeared that SWY-type aluminosilicate zeolites had been successfully prepared. This was named STA-30 (St Andrews microporous material-30). Differences in intensity between the simulated pattern of STA-20 and the observed pattern of STA-30 are thought to arise mainly from their different extra-framework species, but additional proof was required that STA-30 was indeed a zeolite with the SWY topology (see below). For more context, usual differences between the simulated and measured XRD patterns of related zeolites discussed here can be found in the SI, Figure S6.

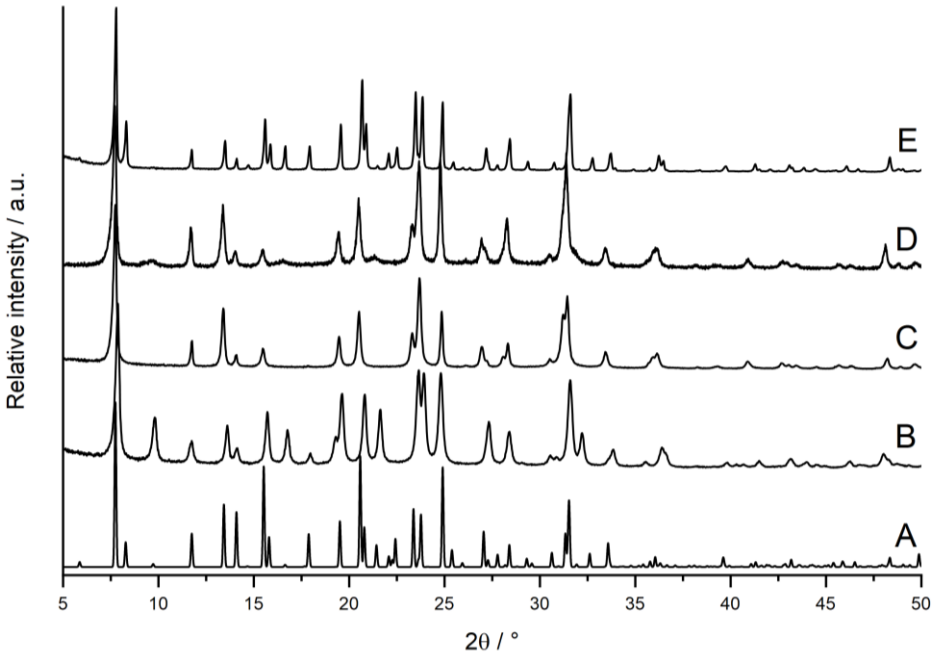

Figure 3. Comparison of the XRD pattern of as-prepared STA-30 (E) compared with the simulated pattern for SAPO STA-20[19] (A) and observed XRD patterns of other related zeolites in as-prepared form: erionite (B), offretite (C) and ZSM-34 (D).

The dependence of the crystallisation on the composition of the gel and other synthetic parameters was investigated taking 398 – 413 K as the preferred temperature range. Additionally, even though the synthesis can be carried out with other tetraalkylammonium solutions (details in the SI, Section 5), the 40% aqueous TPAOH solution was chosen as the preferred base for further testing.

Most significantly, given its importance in determining hydrothermal stability, the Si/Al ratio of the STA-30 could be increased from 5.8 to 7.1 (see Samples 1 and 2 in Table 2) by reducing the amount of Al added to the gel. Further reduction led to no product being formed after 5 days, when the synthesis was performed with Al(o-*i*-Pr)$_3$ in 50 mL tumbling autoclaves.

There is a lower limit to the K^+ content that enables crystallisation of STA-30 to occur (K/Si = 0.05, Sample 3, Table 2), even if the solution alkalinity is kept constant by the addition of more of the hydroxide (rather than the bromide) form of the diDABCO-C8^{2+}. The STA-30 products had levels of ~0.7 K/Al (determined by EDS), which corresponds to a molar ratio of K/Si in the gel of about 0.05, indicating the K was taken up with high specificity. Changing the K^+ content had little effect on the particle morphology (SI, Section 6, Figure S8), in contrast to the effect observed previously for other materials from the ABC-6 family.[49,50] By contrast, reducing the OSDA content by 25% gave crystals with similar morphology but much reduced size (Sample 4 Table 2, Figure 4B). Additionally, other diDABCO-C*n*$^{2+}$, n = 7, 9 and 10, were tested as OSDAs to test the predictions from the computational modelling. While STA-30 was still prepared in all cases, there were some notable differences between the XRD patterns of the products (SI, Section 7, Figure S9). The materials synthesised with diDABCO-C7^{2+} and the longer diDABCO-C*n* molecules were less crystalline than that prepared with diDABCO-C8^{2+} as indicated by elevated background signal in the 20-30° 2θ range of their XRD patterns. This implies that these cations are less effective templates for the *swy* cage than diDABCO-C8^{2+}, in line with the computational data.

Scale up to 125 mL using Al(O-*i*-Pr)$_3$ was successful, giving a material with a lower Si/Al ratio when compared to a similar preparation on the 50 mL scale (Samples 2 and 5 Table 2), without otherwise affecting the product (PXRDs in the SI, Section 7, Figure S10). It was possible to lower the amount of Al(O-*i*-Pr)$_3$ in the gel to obtain a more silica-rich product (Sample 6, Table 2).

Since the method proved to be suitable for synthesis on larger scales, the suitability of Al(OH)$_3$ as the Al source was also investigated, because its use eliminates the need to remove the isopropyl alcohol evolved in the precursor gel formation. Furthermore, Al(O-*i*-Pr)$_3$ is an undesirable Al source commercially because of its high cost. The replacement of the Al(O-*i*-Pr)$_3$ was straightforward on the 125 mL scale (Sample 7, Table 2) as the TPAOH is a strong enough base to dissolve the reagent and

enable successful crystallisation. However, the use of the hydroxide led to lower yields compared to the syntheses carried out with Al(O-*i*-Pr)$_3$. Notably, the Si/Al ratio of the product synthesised with Al(OH)$_3$ was higher than one synthesised with an equivalent amount of Al in the form of Al(O-*i*-Pr)$_3$ (Samples 5 and 7, Table 2). This proved that Al(OH)$_3$ is a viable Al source in this preparation of STA-30, which is further enforced by the successful scale up to a 1.5 L scale without affecting the Si/Al ratio of the product (Sample 8, Table 2) as was observed in the case of Al(o-*i*-Pr)$_3$. Despite the compositional and synthetic differences between the samples discussed in this paragraph, the morphology and size of the crystals of STA-30 were similar to those shown in Figure 4A (~1 μm long rice grain shaped crystallites). Additionally, taking these various optimisations into account, it was possible to synthesise higher Si/Al ratio materials (Si/Al ratio of 7.3, Sample 10 in Table 2), which shows the potential of this method to produce zeolites with controlled chemical compositions.

Table 2. Selection of syntheses related to the preparation of STA-30

		Molar ratio to SiO_2 in the gel[a]					
Sample	**Al source**	**Al_2O_3**	**KOH**	**(diDABCO-C8)Br_2**	**H_2O**	**Scale (mL)**	**Product Si/Al**
1	Al(O-i-Pr)$_3$	0.05	0.10	0.12	20	50	5.8
2	Al(O-i-Pr)$_3$	0.04	0.10	0.12	20	50	7.1
3	Al(O-i-Pr)$_3$	0.04	0.05	0.13	20	50	6.7
4	Al(O-i-Pr)$_3$	0.04	0.08	0.10	20	125	5.5
5	Al(O-i-Pr)$_3$	0.04	0.12	0.13	20	125	5.8
6	Al(O-i-Pr)$_3$	0.03	0.12	0.13	20	125	6.8
7	Al(OH)$_3$	0.04	0.08	0.13	24	125	7.1
8	Al(OH)$_3$	0.04	0.08	0.13	20	1500	7.0
9	Al(OH)$_3$	0.03	0.12	0.13	20	125	6.3
10	Al(OH)$_3$	0.04	0.06	0.09	20	50	7.3

[a] All molar quantities as ratio to 1.0 SiO_2. The TPAOH/SiO_2 molar ratio for all samples was 0.4.

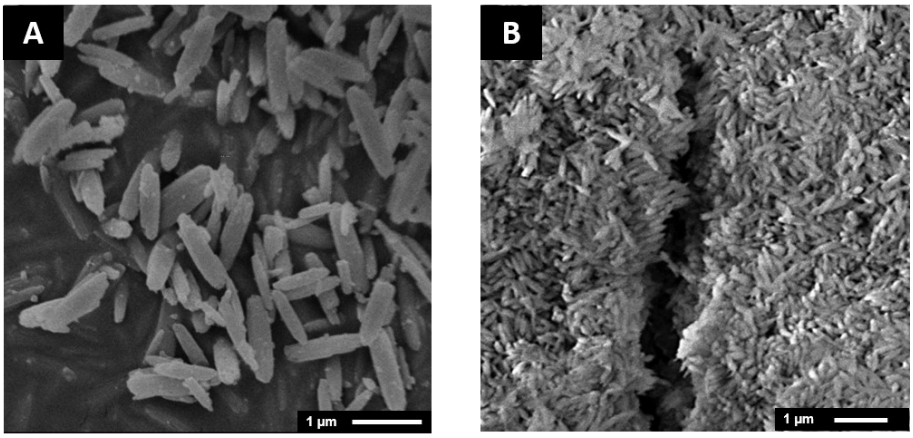

Figure 4. SEM images of Sample 1 (A) and Sample 4 (B).

The ^{13}C, ^{29}Si and ^{27}Al MAS NMR spectra of as-prepared STA-30 (Si/Al = 7.0) are shown in Figure 5. ^{13}C MAS NMR shows that the diDABCO-C8^{2+} molecule is included intact while no significant amount of TPA^{+} is present. The small peak at 11 ppm might indicate that the bulk sample contained trace amounts of TPA^{+} (the other peaks expected around 16 ppm and 60 ppm were not observed) but the low concentrations ruled out TPA^{+} as a template. Hence, diDABCO-C8^{2+} acts as the template while the TPAOH added in the first step of the preparation acts only as a mineraliser. The assignment of peaks in the ^{13}C spectrum was based on 2D NMR experiments carried out on (diDABCO-C8)Br_2 in a D_2O solution (SI, Section 8, Figure S11). The splitting of the resonances of C atoms in the DABCO units (at 46 ppm and 54 ppm) indicates that the end groups on the diDABCO-C8^{2+} are not in equivalent chemical environments within the framework. This splitting is not observed in the ^{13}C NMR spectrum of the molecule in solution. The other spectra confirm the identity of the material as an aluminosilicate zeolite through the characteristic shifts for $Si(OSi)_n(OAl)_{4-n}$ environments in the ^{29}Si MAS NMR spectrum and the characteristic peak due to tetrahedrally coordinated Al in the ^{27}Al MAS NMR spectrum. Deconvolution of the ^{29}Si MAS NMR spectrum and use of Löwenstein's rule to calculate the Si/Al ratio of the material leads to a value much smaller (3.0) than the one determined by EDS or XRF (7.0), which has been previously observed for related frameworks, such as OFF, where the chemical shift of ^{29}Si in crystallographically distinct T-sites is significantly different.[51] Further investigation into the appropriate method for deconvoluting the ^{29}Si peaks was carried out on the activated material, as described below.

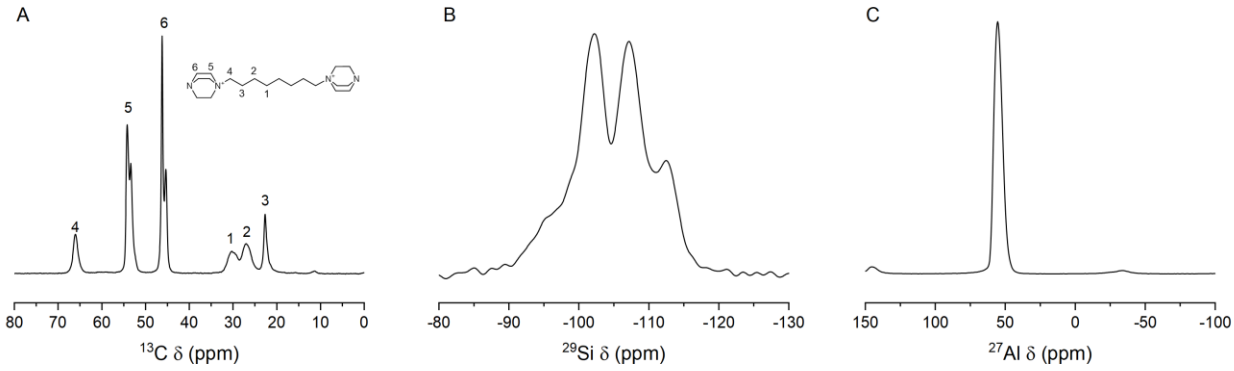

Figure 5. Solid-state MAS NMR data from an as-prepared STA-30 sample: ^{13}C NMR (A), ^{29}Si (B) and ^{27}Al NMR (C).

To prepare porous forms of STA-30, the organic template was removed by calcination in air at 823 K for 12 h, conditions shown by TGA (SI, Section 9, Figure S12) to remove all organics. Additionally, the calcined form was exhaustively ion exchanged with ammonium ions and subsequently deammoniated to the 'activated' form, with a maximum proton content. Notably, while ammonium exchange reduced the K^+ content of the zeolite from ~0.7 K/Al ratio to ~0.3 K/Al, further exchange gave no additional reduction (SI, Section 10). Figure 6 shows that there are some changes in intensity of the peaks between the PXRD patterns of the as-prepared, calcined, and activated materials, but there is no loss in crystallinity, indicating that the H,K-form of STA-30 is thermally stable.

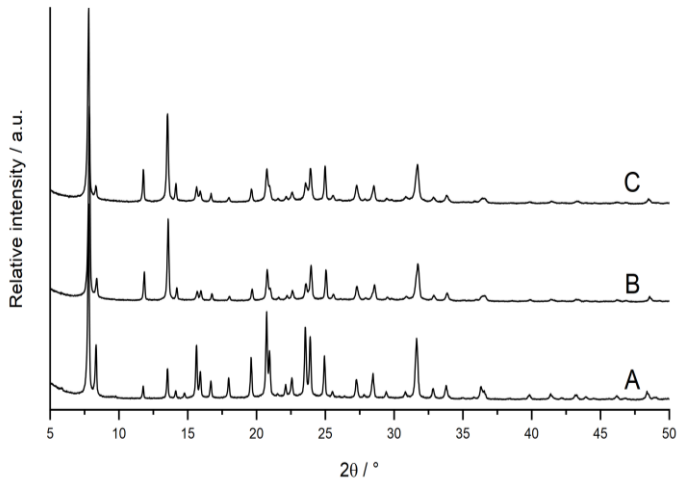

Figure 6. PXRD patterns of as-prepared (A), calcined (B) and activated (C) STA-30.

The crystal structures of the calcined and activated forms, both dehydrated, were determined by Rietveld refinement, using as a starting model an energy-minimised all-silica form of the SWY framework, in space group $P6_3/mmc$. K^+ cation locations and fractional occupancies were refined, to

give good final fits to the observed patterns (Figures 7 and S14). Details of the refinements are given in Tables 3 and 4 and representations of the framework and cation sites shown in Figure 8.

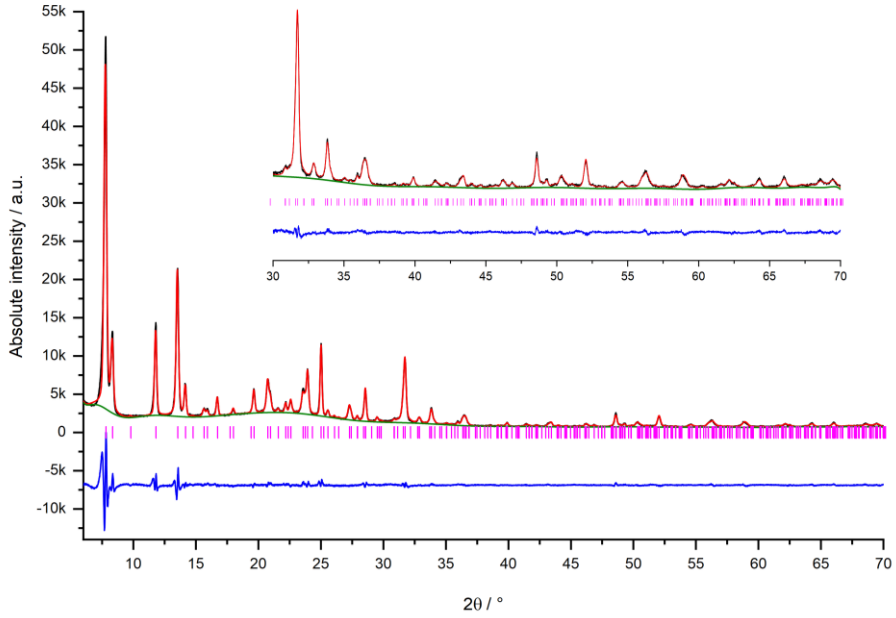

Figure 7. Rietveld plot for dehydrated calcined STA-30. Experimental (black) and calculated (red) PXRD patterns are shown, as well as the fitted background (green), the difference between the observed and calculated patterns (blue) and positions of calculated reflections (pink).

Table 3. Parameters and results of Rietveld refinement performed on STA-30 materials.

Sample	**Calcined, dehydrated**	**Activated, dehydrated**
Expected chemical composition	$H_{3.0}K_{6.1}Al_{9.1}Si_{62.9}O_{144}$	$H_{6.0}K_{3.0}Al_{9.0}Si_{63.0}O_{144}$
Data collection		
Temperature	298 K	298 K
X-Ray source	Cu X-ray tube	Cu X-ray tube
Diffractometer	STOE	STOE
Wavelength / Å	1.54056	1.54056
Unit cell		
Chemical formula	$K_{6.1}Al_{9.1}Si_{62.9}O_{144}$	$K_{2.7}Al_{9.0}Si_{63.0}O_{144}$
Crystal system	Hexagonal	Hexagonal
Space group	$P6_3/mmc$	$P6_3/mmc$
a / Å	13.0647(6)	12.9922(9)
b / Å	13.0647(6)	12.9922(9)
c / Å	29.9577(10)	29.9624(12)
Rietveld refinement		
Refined region / 2θ°	6.0-70.0	6.5-70.0
Background	Chebyshev 24 terms	Chebyshev 30 terms
R_{wp} / %	7.56	4.71
R_p / %	5.10	3.67

Table 4. Structural parameters of the calcined and activated STA-30 samples

Dehydrated calcined STA-30						
Atom	x	y	z	Occupancy	Mult.	U_{iso} (Å^2)
Si/Al1	0.0938(5)	0.4264(5)	0.1251(4)	0.874/0.126	24	0.0232(10)
Si/Al2	1.0019(8)	0.2380(9)	0.1983(4)	0.874/0.126	24	0.0232(10)
Si/Al3	-0.0029(8)	0.2339(9)	0.0521(4)	0.874/0.126	24	0.0232(10)
O1	0.2323(7)	0.4647(15)	0.1228(12)	1.0	12	0.0221(18)
O2	0.0172(16)	0.3446(15)	0.1666(6)	1.0	24	0.0221(18)
O3	0.0785(15)	0.5392(7)	0.1249(13)	1.0	12	0.0221(18)
O4	0.0304(14)	0.3518(14)	0.0801(5)	1.0	24	0.0221(18)
O5	0.1001(12)	0.2002(23)	0.1864(10)	1.0	12	0.0221(18)
O6	0.9984(20)	0.2736(28)	0.25	1.0	12	0.0221(18)
O7	0.8713(11)	0.1287(11)	0.1866(9)	1.0	12	0.0221(18)
O8	0.0992(11)	0.1984(21)	0.0605(10)	1.0	12	0.0221(18)
O9	0	0.2643(28)	0	1.0	12	0.0221(18)
O10	0.8797(10)	0.1203(10)	0.0706(8)	1.0	12	0.0221(18)
K1	0	0	0.8739(21)	0.777(8)	4	0.02995
K2	0.5046(12)	0.4954(12)	0.25	0.495(12)	6	0.11604
Dehydrated activated STA-30						
Atom	x	y	z	Occupancy	Multiplicity	U_{iso}(Å^2)
Si/Al1	0.0900(4)	0.4225(4)	0.12601(31)	0.875/0.125	24	0.0228(8)
Si/Al2	0.9997(6)	0.2389(6)	0.19735(22)	0.875/0.125	24	0.0228(8)
Si/Al3	-0.0024(6)	0.2287(6)	0.05120(24)	0.875/0.125	24	0.0228(8)
O1	0.2256(6)	0.4512(12)	0.1305(7)	1.0	12	0.0179(15)
O2	0.0057(11)	0.3444(11)	0.1668(4)	1.0	24	0.0179(15)
O3	0.0794(13)	0.5397(6)	0.1206(8)	1.0	12	0.0179(15)
O4	0.0316(12)	0.3432(11)	0.0820(4)	1.0	24	0.0179(15)
O5	0.1073(10)	0.2147(20)	0.1859(7)	1.0	12	0.0179(15)
O6	1.0000(17)	0.2634(21)	0.25	1.0	12	0.0179(15)
O7	0.8801(11)	0.1199(11)	0.1836(7)	1.0	12	0.0179(15)
O8	0.0909(6)	0.1818(13)	0.0565(7)	1.0	12	0.0179(15)
O9	0	0.2677(19)	0	1.0	12	0.0179(15)
O10	0.8752(8)	0.1248(8)	0.0710(7)	1.0	12	0.0179(15)
K1	0	0	0.8720(25)	0.668(9)	4	0.10432

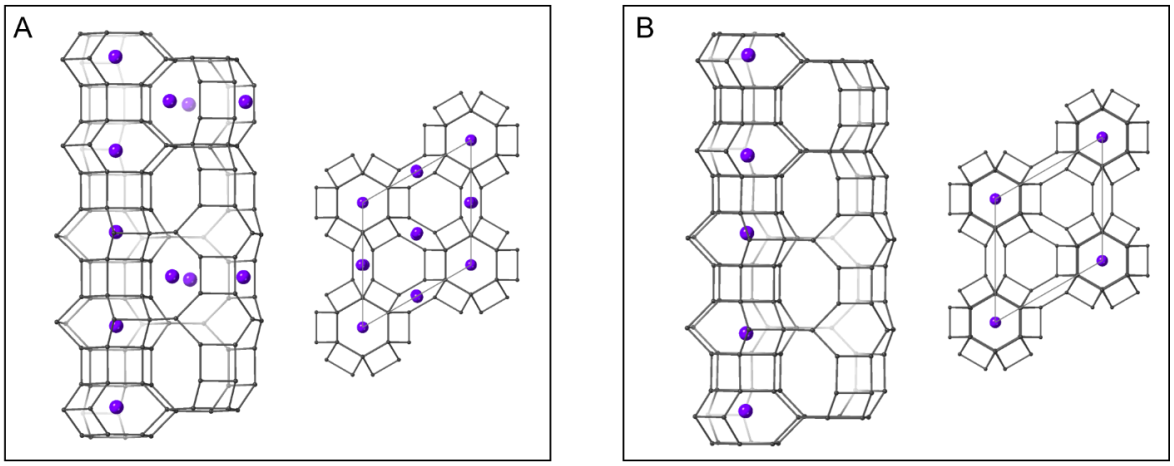

Figure 8. Schematic representation of the structures of dehydrated calcined (A) and activated (B) STA-30, represented with T-T connections and all possible positions for the K^+ cations (purple). O atoms omitted for clarity.

The refinements confirm the structure type of both calcined and activated STA-30 as SWY. Figure 9 shows that the framework contains a column of *can* cages connected by *d6r* units. Additionally, each *swy* cage is connected to three *gme* cages through 8Rs in 'boat' configuration (Figure 9), and to six other *swy* cages through 8Rs in 'chair' configuration (top and bottom of *swy* cage in Figure 9). The 'boat' configuration is characterised by 2 mirror planes, whereas the 'chair' configuration is characterised by a mirror plane and an inversion centre. In calcined STA-30, K^+ cations were located in *can* cages and also in 8R sites between the *gme* cages and *swy* cages (boat-shaped), while the 8R sites between *swy* cages (chair shaped) were not occupied (Figure 10A). The ordering of the K^+ into one of the two types of 8R sites could be due to better coordination in the 'boat' 8R configuration rather than the 'chair' configuration but will also have the effect of minimising cation-cation repulsion. The refinement of the K^+ loading, coupled with the synthetic work described above, shows that the synthesis of a stable STA-30 material depends on the templating of the *can* cages and the occupation of some of the 8R sites, revealing a strong connection between the extra-framework cations and the framework structure. However, it is possible to remove the K^+ cations in these sites without affecting the structure of the material, as shown by the *swy* cage in Figure 10C.

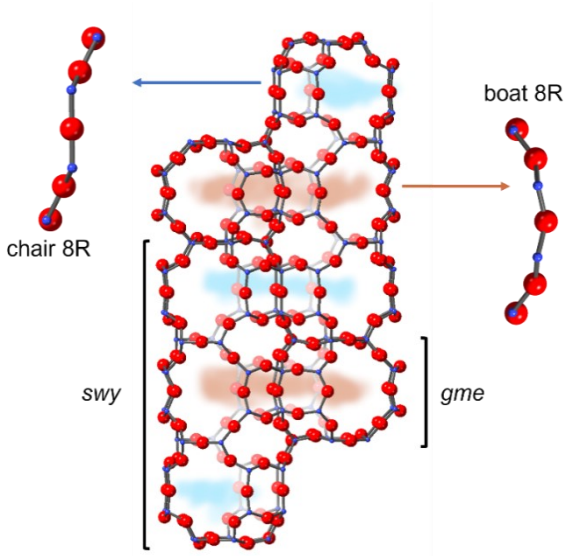

Figure 9. The *swy* and *gme* cages in the framework structure of activated STA-30 material drawn with T-O connections (T atoms – blue, O atoms – red) and showing the connectivity between the cages (blue shading *swy-swy* connectivity through 'chair' 8Rs and brown shading *swy-gme* connectivity through 'boat' 8Rs), the projections across the openings of which are given in the figure.

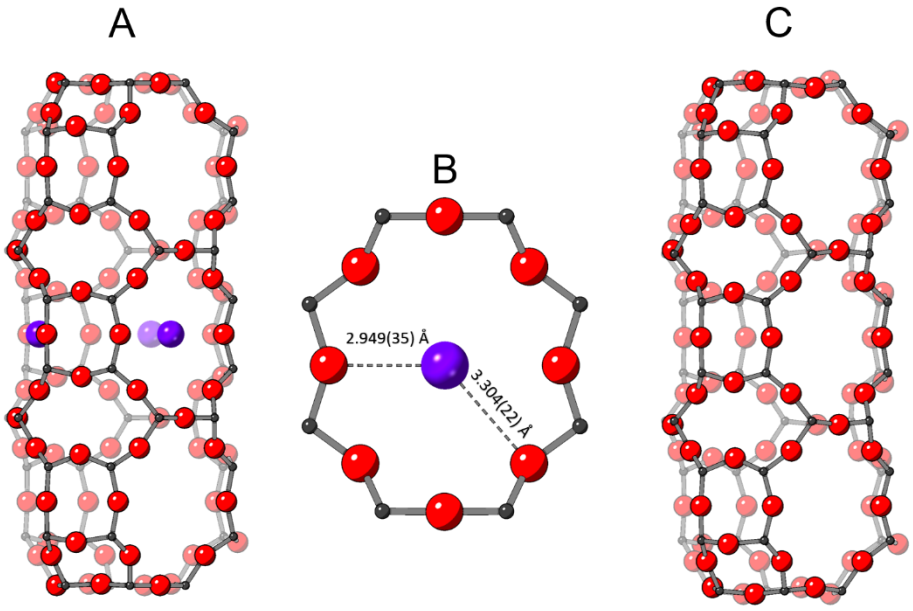

Figure 10. The *swy* cage of calcined STA-30 with the K^+ cation in the boat-shaped 8-ring (A), showed with K-O distances (B) and the *swy* cage of activated STA-30 (C).

In the activated form, there were no K^+ cations in the 8R sites, while the *can* cages remained ~75% occupied. This indicates that while the K^+ cations in the 8R windows were completely removed by ion

exchange with NH_4^+, those in *can* cages could not be removed even if the ion exchange was performed at elevated temperatures (up to 363 K) for many hours. This suggests that, under these conditions at least, the K^+ ions could not escape from the *can* cages because that would require migration through the puckered 6Rs.

The structure of the as-prepared form was also refined, but in this case it was not possible to dehydrate the solid fully without partially decomposing the template, because the presence of the organic prevented diffusion of water molecules out of the structure at temperatures below that at which the template would start to react. The diDABCO-$C8^{2+}$ molecule was included within the *swy* cages in an energy-minimised location in the starting model, and its occupancy allowed to refine. It was found that this had to be capped at a value of 2 molecules/unit cell. K^+ cations were refined at the locations observed in the calcined material, and additional scattering refined as O atoms of water (or OH^- groups). Although some details remained unresolved, the profile fit, and the similarity of unit cell parameters (SI, Section 11, Table S1 and Figure S15) indicate the framework structure of this form is the same as that of the calcined form.

As a complementary structural method, the activated form was investigated by electron microscopy. SAED patterns of the activated material were collected along the [100] direction (Figure 11) which show that there is no disorder in the 12-layer stacking sequence in STA-30 since there is no streaking.[52] High-resolution STEM images (processed with an ABSF filter) along the same zone axis, Figure 11, further confirmed these findings, showing the ordered SWY framework of STA-30 at atomic resolution. A closer observation of the 12-layer stacking sequence is shown inset. These images are also consistent with the SWY topology, as shown by the unbroken columns of *can*/*d6r* units and the strict alternation along the *c*-axis of double combined *can* and *d6r* building units with different orientations along the *b*-axis.

It should also be noted that in the original work on the structure of STA-20, it was shown that two additional hypothetical structure types are possible with similar unit cell parameters (and therefore peak positions) to those of SWY. A comparison of the powder pattern and the electron diffraction pattern of STA-30 with those simulated for the frameworks of these additional phases (coded MS-1 and MS-2 by Turrina *et al.*[19]) indicated that it possessed the SWY topology and not the other, hypothetical, ones (SI, Section 12, Figures S16 and S17).

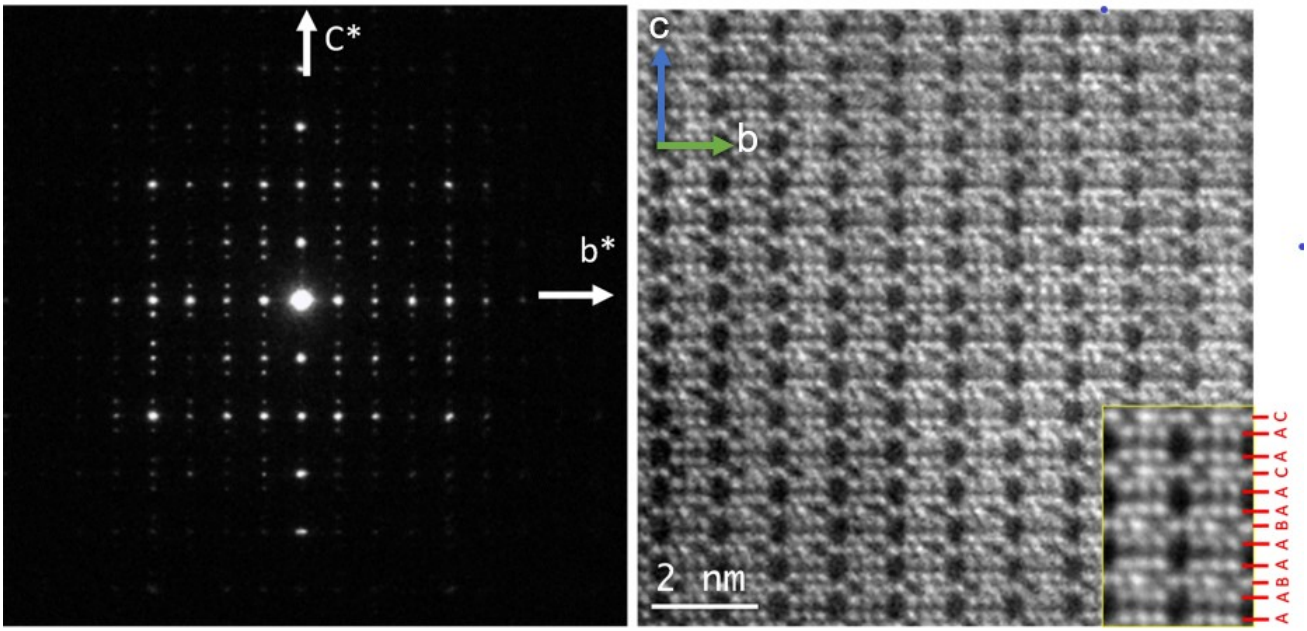

Figure 11. (Left) SAED pattern of STA-30 down the [100] direction and (right) C_s-corrected STEM-ADF image of the framework of STA-30 with arrangement of *can* cages highlighted. A closer observation of the framework is shown inset, where the stacking sequence is marked. The image was processed by application of an ABSF filter.

The composition and reactivity of the aluminosilicate framework of the activated form of STA-30 was investigated further by ^{27}Al, ^{1}H and ^{29}Si MAS NMR (Figure 12).

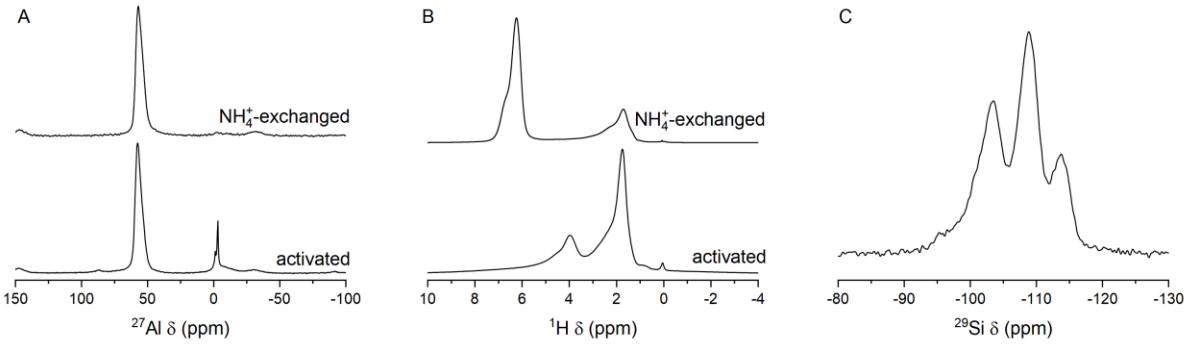

Figure 12. Solid-state MAS NMR data on STA-30: (A) ^{27}Al NMR of hydrated activated (H,K-) and NH_4^+-forms, (B) ^{1}H NMR, dehydrated activated and NH_4^+-forms and (C) ^{29}Si NMR, hydrated H,K-STA-30.

The ^{27}Al MAS NMR of the hydrated activated material shows two well-defined resonances at –2.0 ppm and –3.1 ppm, chemical shifts associated with octahedrally-coordinated Al, as well as the major peak at 57.8 ppm due to the expected tetrahedrally-coordinated framework Al (Figure 12A). The narrow lineshape of the 'octahedral' signals, as well as the absence of any five-fold coordinated signals, argues against these being from extra-framework Al (EFAL) typically observed after hydrothermal treatment, or steaming. It is increasingly becoming apparent that sharp resonances in H-forms of zeolites are more likely to be due to octahedral framework species, formed reversibly from tetrahedral framework Al by the incorporation of water molecules into their coordination shell. [53–55] These species are reported to revert to tetrahedral coordination if the H-zeolites are converted to the ammonium form.[54] Therefore, to investigate whether the octahedral Al in hydrated K,H-STA-30 can also be converted back to tetrahedral species, a sample was ion exchanged into the ammonium form. ^{27}Al NMR of this sample (Figure 12A) shows that the two sharp upfield resonances disappear, strongly suggesting that the coordination of the Al species reverts to tetrahedral. The observation of two distinct signals suggests that these are octahedral framework Al species in different crystallographic sites in the zeolite framework, which to our knowledge has not previously been reported. It is worth noting that there is a very small broad peak around -2.7 ppm present in the ^{27}Al NMR spectrum of the NH_4^+-exchanged sample that can be correlated to a similar feature in the ^{27}Al NMR spectrum of the H-form that overlaps with the sharp peaks. This may indicate the presence of a very small amount of EFAL.

^{1}H NMR spectra from a dehydrated sample of the activated form of the material (Figure 12B) give peaks at 4 ppm and 1.7 ppm. The signal at 4 ppm is assigned, based on previous studies, to Brønsted hydroxyls while the strong signal at 1.7 ppm is similar to previous observations on zeolite Beta and by analogy is assigned as silanol groups, $(SiO)_3SiOH$, indicating an appreciable number of defects in the structure.[56–58]

^{1}H MAS NMR of the NH_4-exchanged form of activated STA-30 (Figure 12B) showed that the Brønsted hydroxyls are removed (as expected) and replaced with ammonium protons (peaks at 6.3 ppm and 6.7 ppm), while the defect hydroxyl groups remain. It was possible to investigate the nature of the 1.7 ppm ^{1}H signal further by ^{1}H–^{29}Si HETCOR spectroscopy on the ammonium-exchanged STA-30 (Figure 13). While the ammonium protons correlate with all the framework Si signals, the hydroxyl protons correlate with a ^{29}Si signal at –102 ppm, which can be attributed to silanol ^{29}Si, $(SiO)_3{}^{29}\underline{Si}OH$.

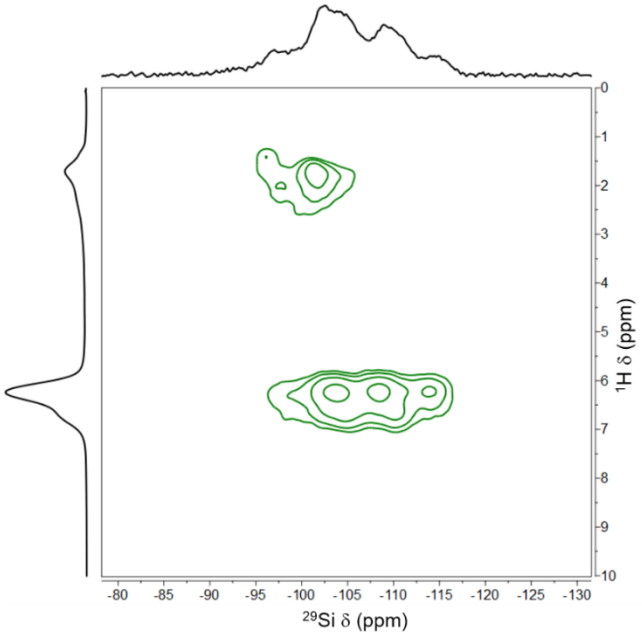

Figure 13. ^{1}H-^{29}Si HETCOR spectrum of the NH_4^+-exchanged STA-30.

Knowing both the crystal structure and the defect structure of the STA-30 it was then possible to analyse the ^{29}Si spectrum of activated STA-30 (Figure 12C). NMR-DFT calculations carried out on an all-silica SWY structural model revealed that the ^{29}Si chemical shift of one of the three crystallographically distinct sites (all of which have the same multiplicity, 24) is expected to be nearly 7 ppm different from the other two, which are magnetically very similar. Resonances are predicted at −114.8 ppm (site T_1) and −108.2 ppm (sites T_2 and T_3) in a ratio of 1:2 (details in the SI, Section 13, Figure S18). Similar differences in ^{29}Si chemical shift are measured (and predicted) for the zeolites offretite and omega (mazzite) for example.[51] Assuming (i) that the ^{29}Si spectrum is composed of two sets of Q^4 peaks of the form $(Si(OSi)_n(OAl)_{4-n}$, n = 0, 1 and 2), one set from each 'group' of similar T-sites, in the ratio 1 (upfield): 2 (downfield), and (ii) that there is a resonance for Q^3 $^{29}SiOH(OSi)_3$ at −100 ppm, it was possible to deconvolute the spectrum and derive a Si/Al ratio of 13±1, close to the value measured by XRF (14.1) (details in SI, Section 13, Figure S19).

Physical properties of activated STA-30

STA-30 was found to be microporous, exhibiting a type I isotherm when adsorbing N_2 at 77 K (Figure 14). The micropore volume was calculated to be 0.31 $cm^3\ g^{-1}$ assuming that the pores were fully filled at p/p_0 = 0.1. This is larger than the micropore volume reported by Łukaszuk *et al.* for aluminosilicate materials with the closely-related OFF topology type (0.25 $cm^3\ g^{-1}$) although that sample also possessed 0.05 $cm^3\ g^{-1}$ of mesopore volume.[50]

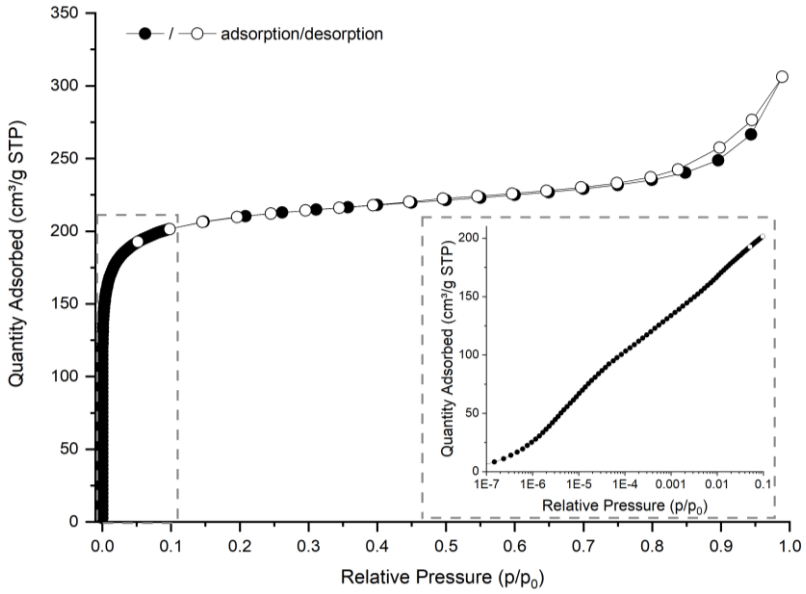

Figure 14. N_2 adsorption at 77 K isotherm measured on the activated H,K-STA-30, shown with an insert focused on the 0 – 0.1 range plotted on a log scale

SCR Catalysis

Small pore zeolites, particularly those with *d6r* units in the ABC-6 family, have been used successfully as commercial catalysts in NO_x abatement technology. Erionite is a zeolite in the ABC-6 family that has shown promising performance due to its high activity and hydrothermal stability.[59,60] Moreover, as discussed previously, ERI shows structural similarity to SWY. Therefore, STA-30 samples with Si/Al ratios of 5.8 and 6.3 (Samples 5 and 9 in Table 2) were synthesized, calcined, and activated according to the methods described and a benchmark synthetic erionite sample of similar Si/Al ratio and morphology was prepared and activated as well (details in SI Section 14). The materials were loaded with 3.33 wt.% Cu cations in extra-framework ion exchange positions as described (Cu-STA-30(5.8), Cu-STA-30(6.3) and Cu-ERI(6.1)). These samples were then investigated as catalysts in NH_3-mediated NO_x reduction to probe the applicability of the aluminosilicate STA-30. Further details on sample preparation and catalyst testing are available in the Experimental section.

The results of the SCR tests are given in Figure 15. Typically, diesel vehicles are calibrated to operate with exhaust gases in the temperature range of 523 – 773 K: previous studies have indicated that the activity of Cu-SSZ-13 for this reaction increases rapidly as temperature increases from 450 to 575 K under similar conditions.[61]

Both STA-30 samples exhibited excellent catalytic activity, achieving greater than 90% NO_x conversion across the entire target operating window (523 – 773 K). Additionally, during cold start conditions, it is beneficial for NO_x abatement catalysts to exhibit low light-off temperatures. A useful metric for quantifying light-off temperature is the T_{50} value, which is the temperature at which 50% NO_x conversion is reached. The Cu-ERI(6.1), Cu-STA-30(6.3), and Cu-STA-30(5.8) samples achieved T_{50} values of about 450, 460, and 470 K, respectively. This might be explained by the Cu:Al ratios of these samples. As reported in a number of studies, Cu:Al ratios approach an ideal value of ~0.5 for Cu-exchanged zeolites utilized as SCR catalysts.[62,63] In Cu-STA-30(5.8) the Cu:Al ratio was 0.22 but taking the K cations in the *can* cages into account, the ratio of Cu: residual framework charge (Al minus K) = 0.31. For Cu-STA-30(6.3) the corresponding ratios are 0.23 and 0.34, a little closer to the optimum value.

The N_2O selectivities of the Cu-loaded STA-30 catalysts were also evaluated (Figure 15B). N_2O is an unwanted by-product of NH_3-mediated NO_x reduction. In emissions control systems for diesel vehicles, it is highly desirable to minimize the production of N_2O because it is a particularly potent greenhouse gas. While increasing the Cu:Al ratio gave a positive effect on NO_x light-off temperature, there is a penalty in N_2O selectivity. Peak N_2O selectivity is increased from 2.5% to 3.5% when the Si/Al ratio of STA-30 SAR is increased from 5.8 to 6.3. A comparison of the ERI reference to STA-30, however, demonstrates that the framework topology of the zeolite can have an impact on N_2O selectivity. The Cu-ERI(6.1) sample exhibited a lower N_2O selectivity at 2.5% relative to the Cu-STA-30(6.3) sample and an equivalent N_2O selectivity to the Cu-STA-30(5.8) sample. These effects demonstrate how zeolite topology, Al content, and Cu content all play major roles in NO_x abatement technology and must be tuned for optimal performance.

These preliminary NH_3-SCR tests indicate Cu-STA-30 exhibits promising activity as an SCR catalyst. As demonstrated for the CHA zeolite as an SCR catalyst, the Cu:Al ratio affects both low temperature NO_x conversion and N_2O selectivity across the entire temperature range.[62–64] The aluminosilicate zeolite STA-30 therefore warrants further investigation and optimization as a NH_3-SCR catalyst.

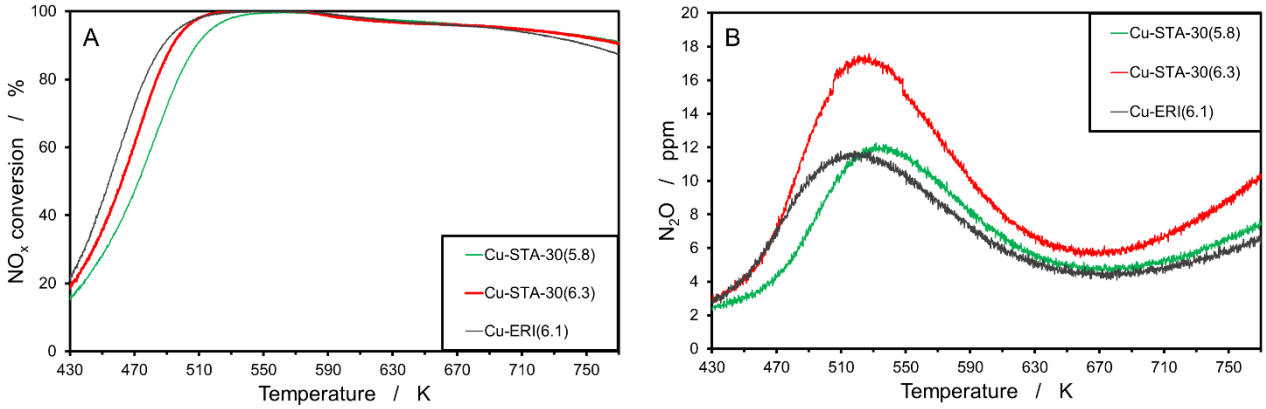

Figure 15. NH_3-SCR light-off curves and N_2O yield plots for Cu-STA-30(5.8), Cu-STA-30(6.3) and Cu-ERI(6.1) samples, which all have a loading of 3.33 wt.% Cu cations.

CONCLUSION

An aluminosilicate zeolite with the SWY topology type (STA-30) has been prepared for the first time, via a designed synthesis involving the selection of organic template by modelling and judicious use of inorganic cations. While the organic alkylammonium diDABCO-C8 dication gives an optimal fit to the *swy* cage (the longest observed in an ordered ABC-6 type zeolite) the K^+ cation favours crystallisation of zeolites that contain *can* cages. The synthesis was tuned to increase the framework Si/Al and optimise stability and modified to permit economical scale up.

Rietveld refinement against PXRD data established that STA-30 has the SWY framework in as-prepared, calcined and activated forms. Selected area diffraction and C_s-corrected STEM imaging confirmed the 12-layer stacking sequence repeat AABAABAACAAC and showed that it is maintained fault-free over extended distances. Parallel columns of alternating *d6r*s and *can* cages run along the *c*-axis in the framework. Between these are alternating *swy* and *gme* cages, connected via 8R windows, which comprise the pore space. In the as-prepared form, diDABCO-C8 cations occupy the *swy* cages, but can be removed by calcination to leave the framework intact. K^+ cations are located in the *can* cages, from which they cannot be removed by ammonium ion exchange, and also 8R windows of the *gme* cages, from which they can.

The calcined, ammonium-exchanged and then deammoniated K,H-form exhibits Brønsted acid sites and defect silanol protons. Upon rehydration of this acid-form, a significant fraction of the framework Al transforms from tetrahedral to octahedral, giving two well resolved narrow resonances in the ^{27}Al NMR. These are interpreted to be octahedral framework Al cations ($Al(OSi)_4(OH_2)_2$) in crystallographically-distinct sites: their coordination can be transformed to tetrahedral by ammonium ion exchange.

The dehydrated K,H-STA-30 shows a microporous volume of 0.31 cm^3 g^{-1}, which indicates the acid form of the zeolite is stable and the pore space, connected via 8R windows, is fully accessible. It is therefore a candidate for conversions known to be catalysed by small pore zeolites: Cu-loaded STA-30 shows appreciable activity for deNO_x. We therefore consider this successful designed synthesis, as a high Si/Al zeolite, of a topology type known previously but as an aluminophosphate, is a promising approach for further catalyst discovery.

Supporting Information

Supporting Information is available free of charge on the ACS Publications website at [doi**********] including: details of organic synthesis; powder X-ray diffraction and crystallographic analysis (including cif files) on hydrated and dehydrated STA-30 and related zeolites; scanning electron micrographs; deconvolution of ^{29}Si MAS NMR and TGA (PDF).

ACKNOWLEDGEMENTS

RGC thanks the University of St Andrews and Johnson Matthey for funding. PAW thanks the EPSRC (Designed Synthesis of Zeolites: EP/S016201/1) and the Royal Society (Industry Fellowship INF\R2\192052) for support. AM acknowledges the Spanish Ministry of Science and Innovation through the Ramon y Cajal programme (RYC2018-024561-I), the Regional government of Aragon (DGA E13_20R) and to the National Natural Science Foundation of China (NFSC-21850410448; NSFC-21835002). Professor Paul A. Cox (University of Portsmouth) is thanked for helpful discussions. AT thanks Rob Fletcher for micropore measurements, Sharron Kenny and David Maclachlan for XRF analyses (Johnson Matthey Analytical Team, Chilton, P.O. Box 1, Belasis Avenue, Billingham, TS23 1LB, United Kingdom). The raw data accompanying this publication are directly available at https://doi.org/10.17630/26349e02-ffbf-4d67-8af2-a96ba325bf9a [reference 65].

REFERENCES

(1) Moliner, M.; Martínez, C.; Corma, A. Synthesis Strategies for Preparing Useful Small Pore Zeolites and Zeotypes for Gas Separations and Catalysis. *Chem. Mater.* **2014**, *26*, 246–258.

(2) Dusselier, M.; Davis, M. E. Small-Pore Zeolites: Synthesis and Catalysis. *Chem. Rev.* **2018**, *118*, 5265–5329.

(3) Kwak, J. H.; Tonkyn, R. G.; Kim, D. H.; Szanyi, J.; Peden, C. H. F. Excellent Activity and Selectivity of Cu-SSZ-13 in the Selective Catalytic Reduction of NO_x with NH_3. *J. Catal.* **2010**, *275*, 187–190.

(4) Beale, A. M.; Gao, F.; Lezcano-Gonzalez, I.; Peden, C. H. F.; Szanyi, J. Recent Advances in Automotive Catalysis for NO_x Emission Control by Small-Pore Microporous Materials. *Chem. Soc. Rev.* **2015**, *44*, 7371–7405.

(5) Moliner, M.; Franch, C.; Palomares, E.; Grill, M.; Corma, A. Cu-SSZ-39, an Active and Hydrothermally Stable Catalyst for the Selective Catalytic Reduction of NO_x. *Chem. Commun.* **2012**, *48*, 8264–8266.

(6) Shan, Y.; Shan, W.; Shi, X.; Du, J.; Yu, Y.; He, H. A Comparative Study of the Activity and Hydrothermal Stability of Al-Rich Cu-SSZ-39 and Cu-SSZ-13. *Appl. Catal. B Environ.* **2020**, *264*, 118511.

(7) Blakeman, P. G.; Burkholder, E. M.; Chen, H.-Y.; Collier, J. E.; Fedeyko, J. M.; Jobson, H.; Rajaram, R. R. The Role of Pore Size on the Thermal Stability of Zeolite Supported Cu SCR Catalysts. *Catal. Today* **2014**, *231*, 56–63.

(8) IZA database http://www.iza-structure.org/databases/ (accessed Oct 8, 2019).

(9) Lee, H.; Choi, W.; Choi, H. J.; Hong, S. B. PST-33: A Four-Layer ABC-6 Zeolite with the Stacking Sequence AABC. *ACS Mater. Lett.* **2020**, 981–985.

(10) Li, Y.; Li, X.; Liu, J.; Duan, F.; Yu, J. In Silico Prediction and Screening of Modular Crystal Structures via a High-Throughput Genomic Approach. *Nat. Commun.* **2015**, *6*, 8328.

(11) Lok, B. M.; Messina, C. A.; Patton, R. L.; Gajek, R. T.; Cannan, T. R.; Flanigen, E. M. Silicoaluminophosphate Molecular Sieves: Another New Class of Microporous Crystalline Inorganic Solids. *J. Am. Chem. Soc.* **1984**, *106*, 6092–6093.

(12) Tian, P.; Wei, Y.; Ye, M.; Liu, Z. Methanol to Olefins (MTO): From Fundamentals to Commercialization. *ACS Catal.* **2015**, *5*, 1922–1938.

(13) Fickel, D. W.; D'Addio, E.; Lauterbach, J. A.; Lobo, R. F. The Ammonia Selective Catalytic Reduction Activity of Copper-Exchanged Small-Pore Zeolites. *Appl. Catal. B Environ.* **2011**, *102*, 441–448.

(14) Wang, A.; Chen, Y.; Walter, E. D.; Washton, N. M.; Mei, D.; Varga, T.; Wang, Y.; Szanyi, J.;

Wang, Y.; Peden, C. H. F.; Gao, F. Unraveling the Mysterious Failure of Cu/SAPO-34 Selective Catalytic Reduction Catalysts. *Nat. Commun.* **2019**, *10*, 1–10.

(15) Wilson, S. T.; Broach, R. W.; Blackwell, C. S.; Bateman, C. A.; McGuire, N. K.; Kirchner, R. M. Synthesis, Characterization and Structure of SAPO-56, a Member of the ABC Double-Six-Ring Family of Materials with Stacking Sequence AABBCCBB. *Microporous Mesoporous Mater.* **1999**, *28*, 125–137.

(16) Zones, S. I. Zeolite SSZ-16. US4508837A, 1985.

(17) Bennett, J. M.; Kirchner, R. M.; Wilson, S. T. Synthesis and Idealized Topology of AlPO4-52, a New Member of the ABC Six-Ring Family. In *Zeolites: Facts, Figures, Future Part A - Proceedings of the 8th International Zeolite Conference*; Jacobs, P. A., van Santen, R. A., Eds.; Elsevier, 1989; Vol. 49, pp 731–739.

(18) Xie, D.; Jensen, O. Molecular Sieve SSZ-112, Its Synthesis and Use. US20190127231A1, 2019.

(19) Turrina, A.; Garcia, R.; Watts, A. E.; Greer, H. F.; Bradley, J.; Zhou, W.; Cox, P. A.; Shannon, M. D.; Mayoral, A.; Casci, J. L.; Wright, P. A. STA-20: An ABC-6 Zeotype Structure Prepared by Co-Templating and Solved via a Hypothetical Structure Database and STEM-ADF Imaging. *Chem. Mater.* **2017**, *29*, 2180–2190.

(20) Deem, M. W.; Pophale, R.; Cheeseman, P. A.; Earl, D. J. Computational Discovery of New Zeolite-Like Materials. *J. Phys. Chem. C* **2009**, *113*, 21353–21360.

(21) Sastre, G.; Cantin, A.; Diaz-Cabañas, M. J.; Corma, A. Searching Organic Structure Directing Agents for the Synthesis of Specific Zeolitic Structures: An Experimentally Tested Computational Study. *Chem. Mater.* **2005**, *17*, 545–552.

(22) Gálvez-Llompart, M.; Cantín, A.; Rey, F.; Sastre, G. Computational Screening of Structure Directing Agents for the Synthesis of Zeolites. A Simplified Model. *Zeitschrift für Krist. - Cryst. Mater.* **2019**, *234*, 451–460.

(23) Kuznetsova, E. D.; Blatova, O. A.; Blatov, V. A. Predicting New Zeolites: A Combination of Thermodynamic and Kinetic Factors. *Chem. Mater.* **2018**, *30*, 2829–2837.

(24) Turrina, A.; Garcia, R.; Cox, P. A.; Casci, J. L.; Wright, P. A. Retrosynthetic Co-Templating Method for the Preparation of Silicoaluminophosphate Molecular Sieves. *Chem. Mater.* **2016**, *28*, 4998–5012.

(25) Simancas, R.; Dari, D.; Velamazan, N.; Navarro, M. T.; Cantin, A.; Jorda, J. L.; Sastre, G.; Corma, A.; Rey, F. Modular Organic Structure-Directing Agents for the Synthesis of Zeolites. *Science* **2010**, *330*, 1219–1222.

(26) Schmidt, J. E.; Deem, M. W.; Davis, M. E. Synthesis of a Specified, Silica Molecular Sieve by Using Computationally Predicted Organic Structure-Directing Agents. *Angew. Chemie Int. Ed.* **2014**, *53*, 8372–8374.

(27) Shi, C.; Li, L.; Yang, L.; Li, Y. Molecular Simulations of Host-Guest Interactions between Zeolite Framework STW and Its Organic Structure-Directing Agents. *Chinese Chem. Lett.* **2020**, *31*, 1951–1955.

(28) Hong, X.; Chen, W.; Zhang, G.; Wu, Q.; Lei, C.; Zhu, Q.; Meng, X.; Han, S.; Zheng, A.; Ma, Y.; Parvulescu, A. N.; Müller, U.; Zhang, W.; Yokoi, T.; Bao, X.; Marler, B.; De Vos, D. E.; Kolb, U.; Xiao, F. S. Direct Synthesis of Aluminosilicate IWR Zeolite from a Strong Interaction between Zeolite Framework and Organic Template. *J. Am. Chem. Soc.* **2019**, *141*, 18318–18324.

(29) Castañeda, R.; Corma, A.; Fornés, V.; Rey, F.; Rius, J. Synthesis of a New Zeolite Structure ITQ-24, with Intersecting 10- and 12-Membered Ring Pores. *J. Am. Chem. Soc.* **2003**, *125*, 7820–7821.

(30) Cantín, A.; Corma, A.; Diaz-Cabanas, M. J.; Jordá, J. L.; Moliner, M. Rational Design and HT Techniques Allow the Synthesis of New IWR Zeolite Polymorphs. *J. Am. Chem. Soc.* **2006**, *128*, 4216–4217.

(31) Jo, D.; Hong, S. B. Targeted Synthesis of a Zeolite with Pre-Established Framework Topology. *Angew. Chemie - Int. Ed.* **2019**, *58*, 13845–13848.

(32) Shin, J.; Jo, D.; Hong, S. B. Rediscovery of the Importance of Inorganic Synthesis Parameters in the Search for New Zeolites. *Acc. Chem. Res.* **2019**, *52*, 1419–1427.

(33) Guo, P.; Shin, J.; Greenaway, A. G.; Min, J. G.; Su, J.; Choi, H. J.; Liu, L.; Cox, P. A.; Hong, S. B.; Wright, P. A.; Zou, X. A Zeolite Family with Expanding Structural Complexity and Embedded Isoreticular Structures. *Nature* **2015**, *524*, 74–78.

(34) Shin, J.; Xu, H.; Seo, S.; Guo, P.; Min, J. G.; Cho, J.; Wright, P. A.; Zou, X.; Hong, S. B. Targeted Synthesis of Two Super-Complex Zeolites with Embedded Isoreticular Structures. *Angew. Chemie Int. Ed.* **2016**, *55*, 4928–4932.

(35) Mitchell, D. R. G. Dave Mitchell's DigitalMicrograph™ Scripting Website http://dmscripting.com/publications.html (accessed May 15, 2019).

(36) Toby, B. H. EXPGUI, a Graphical User Interface for GSAS. *J. Appl. Crystallogr.* **2001**, *34*, 210–213.

(37) Wright, P. A. Microporous Framework Solids. Royal Society of Chemistry: Cambridge 2008, pp 79–147.

(38) CrystalMaker Software Ltd, Version 10.5, O. CrystalMaker. Oxford 2020.

(39) Dassault Systèmes BIOVIA Materials Studio 2020, San Diego: Dassault Systèmes. Dassault Systèmes BIOVIA Materials Studio. San Diego: Dassault Systèmes 2020.

(40) Sun, H. COMPASS: An Ab Initio Force-Field Optimized for Condensed-Phase Applications Overview with Details on Alkane and Benzene Compounds. *J. Phys. Chem. B* **1998**, *102*, 7338–7364.

(41) Sun, H.; Jin, Z.; Yang, C.; Akkermans, R. L. C.; Robertson, S. H.; Spenley, N. A.; Miller, S.; Todd, S. M. COMPASS II: Extended Coverage for Polymer and Drug-like Molecule Databases. *J. Mol. Model.* **2016**, *22*, 1–10.

(42) Clark, S. J.; Segall, M. D.; Pickard, C. J.; Hasnip, P. J.; Probert, M. I. J.; Refson, K.; Payne, M. C. First Principles Methods Using CASTEP. *Zeitschrift für Krist. - Cryst. Mater.* **2005**, *220*, 567–570.

(43) Perdew, J. P.; Burke, K.; Ernzerhof, M. Generalized Gradient Approximation Made Simple. *Phys. Rev. Lett.* **1996**, *77*, 3865–3868.

(44) Tkatchenko, A.; Scheffler, M. Accurate Molecular van Der Waals Interactions from Ground-State Electron Density and Free-Atom Reference Data. *Phys. Rev. Lett.* **2009**, *102*, 6–9.

(45) Monkhorst, H. J.; Pack, J. D. Special Points for Brillouin-Zone Integrations. *Phys. Rev. B* **1976**, *13*, 5188–5192.

(46) Bonhomme, C.; Gervais, C.; Babonneau, F.; Coelho, C.; Pourpoint, F.; Azaïs, T.; Ashbrook, S. E.; Griffin, J. M.; Yates, J. R.; Mauri, F.; Pickard, C. J. First-Principles Calculation of NMR Parameters Using the Gauge Including Projector Augmented Wave Method: A Chemist's Point of View. *Chem. Rev.* **2012**, *112*, 5733–5779.

(47) Zhu, J.; Liu, Z.; Iyoki, K.; Anand, C.; Yoshida, K.; Sasaki, Y.; Sukenaga, S.; Ando, M.; Shibata,

H.; Okubo, T.; Wakihara, T. Ultrafast Synthesis of High-Silica Erionite Zeolites with Improved Hydrothermal Stability. *Chem. Commun.* **2017**, *53*, 6796–6799.

(48) Burkett, S. L.; Davis, M. E. Mechanisms of Structure Direction in the Synthesis of Pure-Silica Zeolites. 1. Synthesis of TPA/Si-ZSM-5. *Chem. Mater.* **1995**, *7*, 920–928.

(49) Miller, M. A.; Lewis, G. J.; Moscoso, J. G.; Koster, S.; Modica, F.; Gatter, M. G.; Nemeth, L. T. Synthesis and Catalytic Activity of UZM-12. *Stud. Surf. Sci. Catal.* **2007**, *170*, 487–492.

(50) Łukaszuk, K. A.; Rojo-Gama, D.; Øien-Ødegaard, S.; Lazzarini, A.; Berlier, G.; Bordiga, S.; Lillerud, K. P.; Olsbye, U.; Beato, P.; Lundegaard, L. F.; Svelle, S. Zeolite Morphology and Catalyst Performance: Conversion of Methanol to Hydrocarbons over Offretite. *Catal. Sci. Technol.* **2017**, *7*, 5435–5447.

(51) Fyfe, C. A.; Gobbi, G. C.; Kennedy, G. J.; Graham, J. D.; Ozubko, R. S.; Murphy, W. J.; Bothner-By, A.; Dadok, J.; Chesnick, A. S. Detailed Interpretation of the ^{29}Si and ^{27}Al High-Field MAS n.m.r. Spectra of Zeolites Offretite and Omega. *Zeolites* **1985**, *5*, 179–183.

(52) Cowley, J. M. Diffuse Scattering and Absorption Effects. In *Diffraction Physics*; Elsevier, 1995; pp 257–285.

(53) Wouters, B. H.; Chen, T.-H.; Grobet, P. J. Reversible Tetrahedral−Octahedral Framework Aluminum Transformation in Zeolite Y. *J. Am. Chem. Soc.* **1998**, *120*, 11419–11425.

(54) Ravi, M.; Sushkevich, V. L.; van Bokhoven, J. A. Lewis Acidity Inherent to the Framework of Zeolite Mordenite. *J. Phys. Chem. C* **2019**, *123*, 15139–15144.

(55) Ravi, M.; Sushkevich, V. L.; van Bokhoven, J. A. Towards a Better Understanding of Lewis Acidic Aluminium in Zeolites. *Nat. Mater.* **2020**, *19*, 1047–1056.

(56) Gabrienko, A. A.; Danilova, I. G.; Arzumanov, S. S.; Toktarev, A. V; Freude, D.; Stepanov, A. G. Strong Acidity of Silanol Groups of Zeolite Beta: Evidence from the Studies by IR Spectroscopy of Adsorbed CO and ^{1}H MAS NMR. *Microporous Mesoporous Mater.* **2010**, *131*, 210–216.

(57) Hunger, M.; Ernst, S.; Steuernagel, S.; Weitkamp, J. High-Field ^{1}H MAS NMR Investigations of Acidic and Non-Acidic Hydroxyl Groups in Zeolites H-Beta, H-ZSM-5, H-ZSM-58 and H-MCM-22. *Microporous Mater.* **1996**, *6*, 349–353.

(58) Stepanov, A. G. Chapter 4 - Basics of Solid-State NMR for Application in Zeolite Science:

Material and Reaction Characterization; Sels, B. F., Kustov, L. M. B. T.-Z. and Z.-L. M., Eds.; Elsevier: Amsterdam, 2016; pp 137–188.

(59) Martín, N.; Paris, C.; Vennestrøm, P. N. R.; Thøgersen, J. R.; Moliner, M.; Corma, A. Cage-Based Small-Pore Catalysts for NH_3-SCR Prepared by Combining Bulky Organic Structure Directing Agents with Modified Zeolites as Reagents. *Appl. Catal. B Environ.* **2017**, *217*, 125–136.

(60) Zhu, J.; Liu, Z.; Xu, L.; Ohnishi, T.; Yanaba, Y.; Ogura, M.; Wakihara, T.; Okubo, T. Understanding the High Hydrothermal Stability and NH_3-SCR Activity of the Fast-Synthesized ERI Zeolite. *J. Catal.* **2020**, *391*, 346–356.

(61) Kwak, J. H.; Tran, D.; Szanyi, J.; Peden, C. H. F.; Lee, J. H. The Effect of Copper Loading on the Selective Catalytic Reduction of Nitric Oxide by Ammonia over Cu-SSZ-13. *Catal. Letters* **2012**, *142*, 295–301.

(62) Gao, F.; Washton, N. M.; Wang, Y.; Kollár, M.; Szanyi, J.; Peden, C. H. F. Effects of Si/Al Ratio on Cu/SSZ-13 NH_3-SCR Catalysts: Implications for the Active Cu Species and the Roles of Brønsted Acidity. *J. Catal.* **2015**, *331*, 25–38.

(63) Ryu, T.; Kim, H.; Hong, S. B. Nature of Active Sites in Cu-LTA NH_3-SCR Catalysts: A Comparative Study with Cu-SSZ-13. *Appl. Catal. B Environ.* **2019**, *245*, 513–521.

(64) Gao, F.; Walter, E. D.; Kollar, M.; Wang, Y.; Szanyi, J.; Peden, C. H. F. Understanding Ammonia Selective Catalytic Reduction Kinetics over Cu/SSZ-13 from Motion of the Cu Ions. *J. Catal.* **2014**, *319*, 1–14.

(65) Chitac, R. G.; Bradley, J.; McNamara N.; Mayoral, A.; Turrina, A.; Wright, P. A. **2021**. Designed Synthesis of STA-30: A Small Pore Zeolite Catalyst with Topology Type SWY (dataset). University of St Andrews Portal. https://doi.org/10.17630/26349e02-ffbf-4d67-8af2-a96ba325bf9a

Designed Synthesis of STA-30: A Small Pore Zeolite Catalyst with Topology Type SWY

Ruxandra G. Chitac, Jonathan Bradley, Nicholas McNamara, Alvaro Mayoral, Alessandro Turrina and Paul A. Wright